

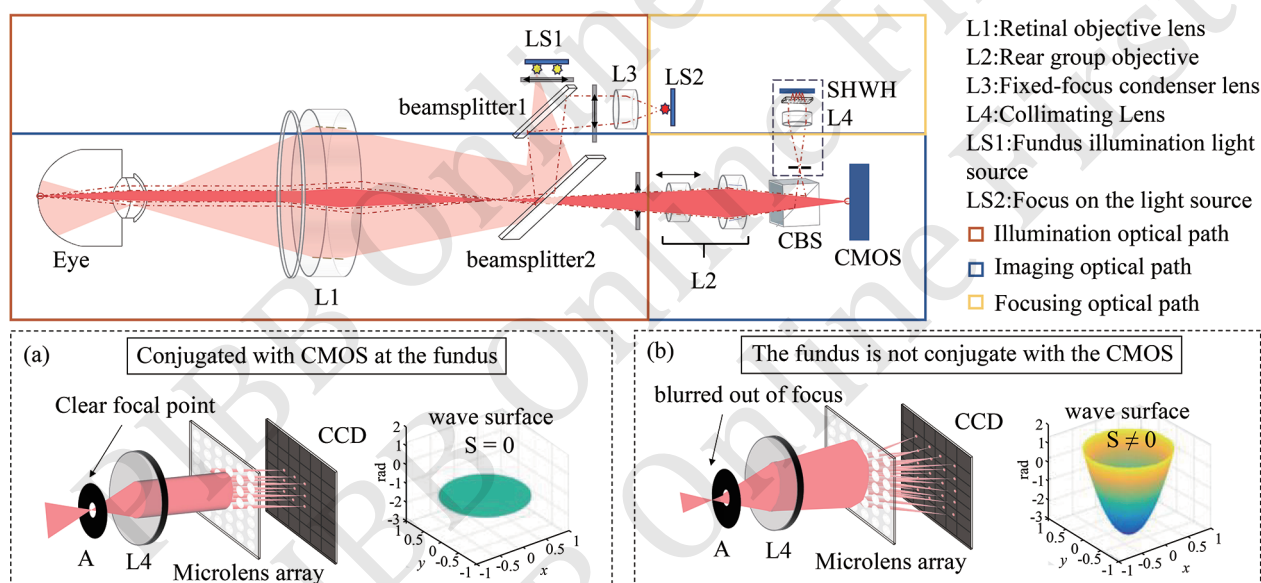


# Compact Fundus Imaging System Using Shack–Hartmann Wavefront Sensing for High-speed Auto-focus\*

CHEN Long\*\*, LIN Zhe-Kai\*\*, ZHENG Geng-Yong, HUANG Jin-Tian, DONG Jia-Xin, YANG Shang-Pan, DING Wen-Zheng, ZENG Ya-Guang, WANG Xue-Hua\*\*\*, HAN Ding-An\*\*\*

(School of Physics and Optoelectronic Engineering, Foshan University, Foshan 528225, China)

## Graphical abstract



**Abstract Objective** The widespread adoption of portable fundus cameras for primary care and community screening is hindered by limitations in current autofocus (AF) technologies. Image-based methods relying on sharpness evaluation require iterative searches, resulting in slow convergence, while projection-based techniques are susceptible to optical artifacts and calibration errors. To address these challenges, this study introduces a novel AF system based on direct wavefront sensing, designed to deliver simultaneous high speed, high precision, and operational robustness within the compact form factor essential for portable ophthalmic

\* This work was supported by grants from The National Natural Science Foundation of China (62205060, 62075042) and the Research Fund of the Joint Laboratory for Intelligent Micro-Nano Optoelectronic Technology of Guangdong, Hong Kong and Macao (2020B1212030010).

\*\* These authors contributed equally to this work.

\*\*\* Corresponding author.

WANG Xue-Hua. Tel: 86-18718560259, E-mail: xhwang10000@163.com

HAN Ding-An. Tel: 86-15118799767, E-mail: handingan@163.com

Received: November 5, 2025 Accepted: February 11, 2026

devices. **Methods** Our approach fundamentally reimagines the AF process by directly measuring the ocular wavefront aberration. We developed a custom portable fundus camera integrating a miniaturized Shack-Hartmann wavefront sensor (SHWS) into the optical path. An 850 nm laser diode projects a point source onto the retina *via* oblique illumination to minimize corneal reflections. Light scattered from this spot carries the eye's refractive error through the imaging optics and is directed to the SHWS, positioned at a plane optically conjugate to the primary color CMOS imaging sensor. A microlens array within the SHWS samples the incident wavefront, generating a pattern of focal spots on a CCD. Real-time centroid analysis of these spots provides a map of local wavefront slopes. These measurements are processed through a singular value decomposition (SVD) algorithm to fit a Zernike polynomial basis set, enabling real-time reconstruction of the wavefront phase. The defocus component (S) is extracted from the second-order Zernike coefficients, providing a direct, quantitative measure of the refractive error in diopters. This value serves as a precise error signal in a closed-loop control system, which commands a voice-coil actuated focusing lens to its null position in a single, deterministic step, eliminating the need for iterative search algorithms. **Results** Comprehensive evaluation demonstrated the system's high performance. Testing on a calibrated model eye (OEMI-7) established a highly linear relationship between the computed defocus S and the focusing lens position across a  $\pm 20$  Diopter (D) compensation range, achievable within a 5 mm mechanical travel. The system achieved a focusing precision of 0.08 D, corresponding to an 18-fold improvement over a conventional projection spot-size method tested under identical conditions. The total focus acquisition time, encompassing wavefront measurement, computation, and lens actuation, averaged under 0.5 s. Clinical validation with 25 human volunteers (50 eyes, refractive range - 15 D to +10 D) confirmed practical efficacy. The wavefront-sensing AF succeeded in 92% of attempts with a mean time of 0.5 s, substantially outperforming a projection-based benchmark which achieved only a 32% success rate with an average time of 4.25 s. The system provided instantaneous directional guidance and maintained stability during minor ocular movements. Objective assessment of image quality, via amplitude contrast of retinal vasculature, showed consistent and significant enhancement following AF correction across the entire tested diopter range. **Conclusion** This work successfully implements and validates a direct wavefront-sensing autofocus paradigm for portable fundus cameras. By directly quantifying and compensating for the optical defocus aberration, this method bypasses the fundamental limitations of image-processing and projection-based techniques, enabling rapid, precise, and deterministic diopter compensation. The developed system delivers an exceptional combination of a wide operational range ( $\pm 20$  D), high accuracy (0.08 D), fast convergence (0.5 s), and a compact physical footprint. This technology provides a practical and high-performance focusing solution capable of enhancing the reliability, throughput, and diagnostic utility of portable retinal imaging in large-scale screening applications. Future efforts will be directed towards system cost optimization and performance adaptation for diverse ocular conditions.

**Key words** portable fundus camera, autofocus, wavefront detection, Shack-Hartmann wavefront sensor

**DOI:** 10.3724/j.pibb.2025.0491

**CSTR:** 32369.14.pibb.20250491

Portable fundus cameras are increasingly used for large-scale screening in the community due to their compact size, ease of operation, and low cost. However, to keep costs down, these devices often employ rolling-shutter cameras that demand fast autofocus capability. Consequently, imaging performance relies heavily on the accuracy and speed of the autofocus system<sup>[1-3]</sup>.

Early portable fundus cameras required manual adjustment, where operators subjectively assessed vessel clarity in near-infrared images<sup>[4-5]</sup>. This method suffers from poor repeatability and low accuracy. Several autofocus strategies have been developed to address these issues, yet each has notable limitations. Image processing-based techniques, such as coarse-to-fine sharpness evaluation<sup>[6-7]</sup> and adaptive focus

windows<sup>[8]</sup>, rely on iterative searches that slow down the focusing process. Methods using dual-wavelength illumination with pre-computed lookup tables<sup>[9]</sup> reduce computational load but are sensitive to calibration errors and individual variations. Projection-based approaches, including structured illumination with rings<sup>[10]</sup> or oblique beams<sup>[11]</sup>, are vulnerable to diffraction artifacts and stray light, which compromise reliability and accuracy. Overall, existing solutions have difficulty simultaneously optimizing speed, precision, and system complexity, which impedes progress in portable fundus imaging.

Optical wavefront sensing has emerged as a promising alternative. The Shack-Hartmann wavefront sensor (SHWS) is well established for measuring ocular aberrations and refractive error<sup>[12-15]</sup>.

For example, in adaptive optics scanning laser ophthalmoscopy, the SHWS enables high-resolution imaging by quantifying ocular wavefront aberrations in real time and performing dynamic compensation with a deformable mirror. Similarly, in focus-tunable adaptive optics scanning laser fundus imaging systems, integrated configurations of Badal optics, deformable mirrors, and SHWS have been used to automatically correct low-order ocular aberrations<sup>[16-18]</sup>. In high-order adaptive optics (AO) fundus imaging systems, Li *et al.*<sup>[19]</sup> designed an AO fundus camera that includes a step where the human eye is induced to focus on a visual target to compensate for primary aberrations. However, such systems typically integrate complex and expensive optical components, such as deformable mirrors, aiming to achieve cellular-level ultra-high-resolution imaging. The system's complexity, size, and cost make it unsuitable for portable, fast, and low-cost screening-oriented fundus cameras.

In this work, we propose a wavefront-based autofocus method specifically designed for portable fundus cameras. A miniaturized SHWS with an integrated collimating lens is embedded in the imaging path, allowing direct measurement of wavefront from retinal. The degree of defocus is quantitatively determined by Zernike polynomial and used to drive a focusing lens in a closed-loop manner. This approach eliminates the need for image-quality evaluation, projection-based calibration, or intensive computation. Experimental results show that the system provides  $\pm 20$  Diopter (D) of refractive compensation over a 5 mm focusing range, with an accuracy of 0.08 D and full focus acquisition in under 500 ms. Furthermore, the sign of defocus provides

immediate directional guidance, which further enhances focusing efficiency. By integrating high precision, high speed, and a compact design, the proposed system offers a practical solution for automated imaging in portable fundus cameras.

## 1 Layout of optical system

Figure 1 presents the optical layout of the proposed portable fundus camera, which combines fundus imaging with wavefront-based autofocus in a compact configuration. The system comprises two main functional modules: the fundus imaging module and the autofocus module.

The fundus imaging module comprises an illumination path and an imaging path. In the illumination path, light from four white-light LEDs is linearly polarized, directed through a beam splitter and an eyepiece, and forms 4 discrete entrance pupils at the pupil plane to uniformly illuminate the retina. The returning light reflected from the fundus travels back along the imaging path, passes through a focusing lens and a rear objective group, and is then transmitted by a dichroic prism to form a retinal image on a complementary metal-oxide-semiconductor (CMOS) sensor.

The autofocus module comprises a projection path and a wavefront sensing path. In the projection path, an 850 nm laser diode is collimated and directed obliquely into the eye through a projection lens and the eyepiece, generating a point source on the retina. Diffusely reflected light from this spot is collected by the imaging optics, reflected off the dichroic prism, and converged to a conjugate focal point relative to the CMOS plane. This beam subsequently enters the

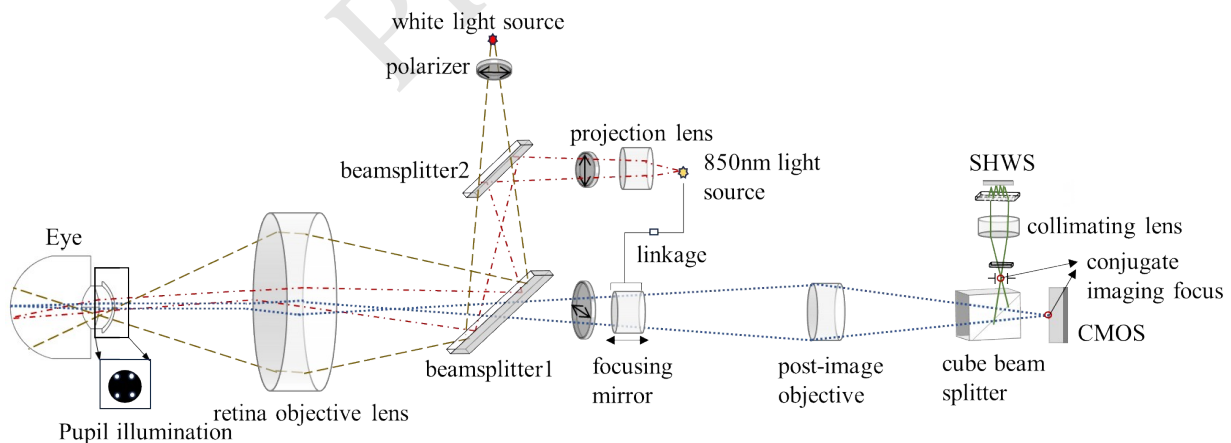


Fig. 1 Optical system for a compact fundus camera based on wavefront detection.

wavefront sensing path, where a spot array is produced for wavefront analysis.

## 2 Principles of auto-focusing via wavefront detection

When the reflected retinal light is focused on the CMOS, the conjugate wavefront approximates a plane wave, producing a uniform and regular spot pattern on the SHWS (A in Figure 2a), Geometrically represented as a plane wave (A in Figure 2c). Conversely, under defocused conditions, the wavefront becomes aberrated, resulting in an irregular and dispersed spot distribution (B in Figure 2a), Geometrically represented as a convex wave (B in Figure 2c). The system is designed to correct the aberrated wavefront (B) toward the planar reference state (A), thereby providing a quantitative measure for determining the required displacement of the focusing lens.

The wavefront aberration  $W(x,y)$  between states A and B can be expanded as:

$$W(x,y) = \sum_{i=0}^n c_i Z_i(x,y) \quad (1)$$

where  $n$  is the total number of Zernike terms,  $Z_i(x,y)$  denotes the  $i^{th}$  Zernike polynomial<sup>[20]</sup>, and  $c_i$  represents the corresponding Zernike coefficient, The Zernike polynomials are presented in Table S1. According to the geometric principle illustrated in Figure 2b, the wavefront slope can therefore be expressed as the ratio of the centroid displacement to the focal length, which also equals to the partial derivative of the wavefront aberration:

$$\begin{cases} \frac{\delta x}{f} = \frac{\partial \sum_{i=0}^n c_i Z_i(x,y)}{\partial x} \\ \frac{\delta y}{f} = \frac{\partial \sum_{i=0}^n c_i Z_i(x,y)}{\partial y} \end{cases} \quad (2)$$

where  $\delta x$  and  $\delta y$  are the centroid displacements of the spot in the  $x$ - and  $y$ -directions, respectively, and  $f$  is the focal length of an individual microlens.

For a microlens array with  $m$  subapertures, the relationship between the measured wavefront slopes and the Zernike coefficients (using the first  $N$  terms) can be written in matrix form as:

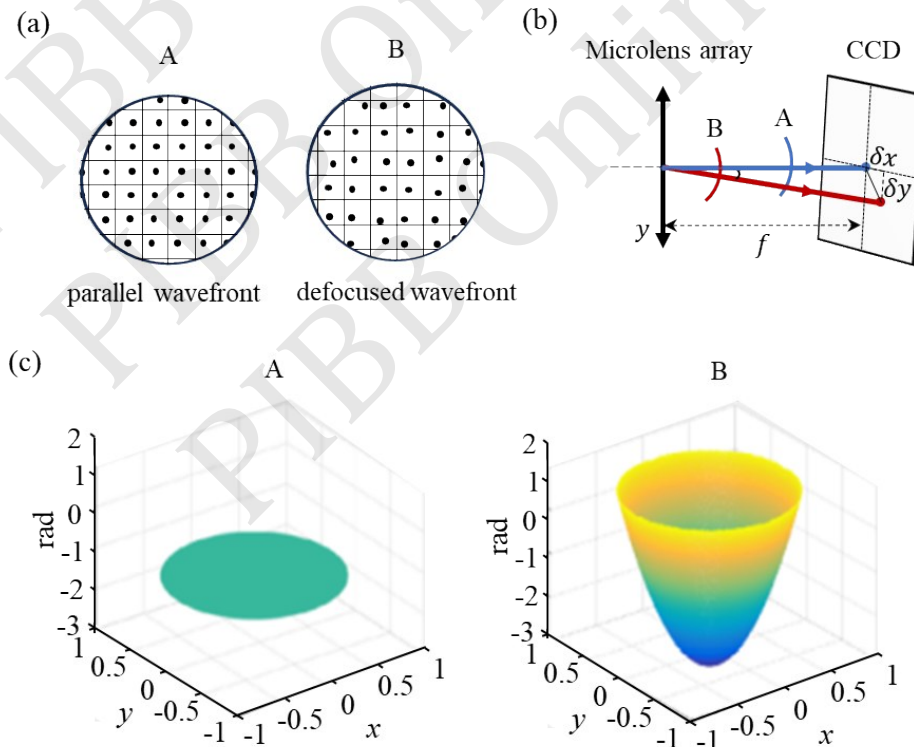


**Fig. 2 Principles of auto-focusing via wavefront detection**

(a) Lattice distribution of parallel wavefront A and defocused wavefront B on the sensor; (b) geometric relationship between the wavefront and CCD under a single microlens; (c) wavefront reconstruction map of parallel wavefront A and defocused wavefront B.

$$\begin{bmatrix} \frac{\delta x_1}{f} \\ \dots \\ \frac{\delta x_m}{f} \\ \frac{\delta y_1}{f} \\ \dots \\ \frac{\delta y_m}{f} \end{bmatrix} = \begin{bmatrix} \frac{\delta Z_1(x_1, y_1)}{\delta x} & \dots & \frac{\delta Z_N(x_1, y_1)}{\delta x} \\ \dots & \dots & \dots \\ \frac{\delta Z_1(x_m, y_m)}{\delta x} & \dots & \frac{\delta Z_N(x_m, y_m)}{\delta x} \\ \frac{\delta Z_1(x_1, y_1)}{\delta y} & \dots & \frac{\delta Z_N(x_1, y_1)}{\delta y} \\ \dots & \dots & \dots \\ \frac{\delta Z_1(x_m, y_m)}{\delta y} & \dots & \frac{\delta Z_N(x_m, y_m)}{\delta y} \end{bmatrix} \cdot \begin{bmatrix} c_1 \\ c_2 \\ \dots \\ c_N \end{bmatrix} \quad (3)$$

This relationship can be expressed in the simplified form  $G = Z \cdot C$ , where  $G$  denotes the slope matrix derived from the measured spot pattern, and  $C$  is the vector of Zernike coefficient. The generalized inverse  $Z^+$  of matrix  $Z$  is obtained *via* singular value decomposition (SVD)<sup>[21]</sup>. The minimal-norm solution for  $C$  in the least-squares sense is then given by:

$$C = Z^+ \cdot G \quad (4)$$

The wavefront can subsequently be reconstructed using Equation (1). Finally, based on the definition of Zernike aberrations, the wavefront defocus  $S$  is calculated from the second-order Zernike coefficients<sup>[22]</sup>:

$$S = -\frac{4\sqrt{3}c_2^0}{R^2} - \frac{2\sqrt{6}\sqrt{(c_2^{-2})^2 + (c_2^2)^2}}{R^2} \quad (5)$$

where  $c_2^0$ ,  $c_2^{-2}$ , and  $c_2^2$  are the second-order Zernike coefficients representing defocus, tilt astigmatism, and 45° astigmatism, respectively, and  $R$  is the pupil radius. The quantity  $S$  quantifies the defocus component of the wavefront aberration and provides a quantitative reference for defocus compensation.

### 3 Optical design and system

Figure 3a shows the overall optical layout of the proposed fundus camera. To implement wavefront-based autofocus while ensuring consistent imaging performance between the white-light and near-infrared (NIR) channels, an internal focusing configuration is employed.

As indicated in Figure 3b, the modulation transfer function (MTF) of the white-light channel exceeds 0.2 at 145 lp/mm across all field positions. The NIR channel achieves comparable performance, with its MTF also surpassing 0.2 at the same spatial frequency (Figure 3c), thereby ensuring an accurate transfer of the NIR-determined focus to the white-

light imaging plane.

To suppress stray-light effects, an oblique illumination scheme is adopted in the projection path. The MTF and spot diagram of this path, presented in Figure 3d, e respectively, demonstrate good optical quality and confirm the ability to form a high-contrast focal spot on the retina.

The wavefront-sensing system integrates a collimating lens, a microlens array, and a charge-coupled device (CCD) sensor. The microlens array is composed of unit lenses with a diameter of 0.4 mm, providing a total clear aperture of 6.8 mm×6.8 mm. This design offers a large receiving area while maintaining high spatial resolution for wavefront sampling. A collimating lens with a 27 mm focal length generates a collimated beam approximately 5.5 mm in diameter, which fully covers the microlens aperture and supplies well-collimated illumination to the CMOS conjugate plane.

A 5-megapixel Magnum MI5100 CCD with a 1/2.5-inch optical format was used as the wavefront detector. Mounted on a 32 mm×32 mm camera board, it provided high-resolution spot imaging in a compact footprint.

Key design parameters of the finalized system are summarized in Table 1. The optical system has a total track length of 190 mm, a 53° field of view, and a diopter compensation range of ±20 D. With an MTF value exceeding 0.3 at 145 lp/mm, the system meets the performance requirements for portable fundus camera applications.

Following the proposed system architecture and design principles, a prototype fundus camera was constructed for experimental validation. As shown in Figure 4, the prototype measures 90 mm in height and 230.4 mm in length, satisfying the portability requirements for clinical screening use.

## 4 Experimental results

### 4.1 Model experiments

A calibration curve relating the defocus value  $S$  to the focusing lens position was first established using an ocular model (OEMI-7-Ocular, Ocular-Model)<sup>[23]</sup>, which closely replicates human eye anatomy and optics.

The imaging path was initially adjusted to maximize vascular contrast, producing a clear fundus image (Figure 5a). In this focused state, the retinal

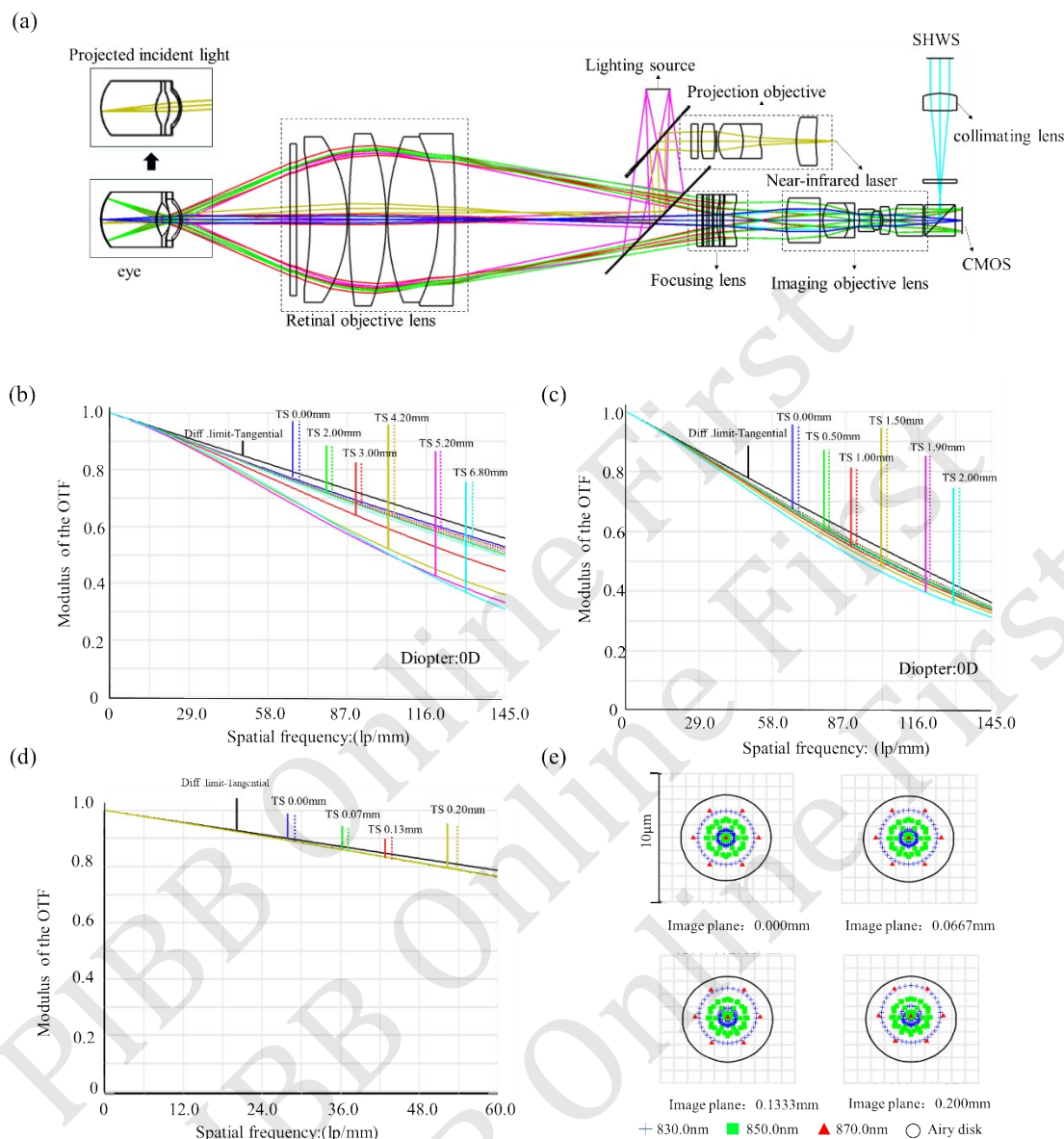


**Fig. 3 Results of the fundus camera optical system design based on wavefront detection**

(a) Final structure of the system optical design. (b) Modulation transfer function of white light imaging in each field of view. (c) Modulation transfer function of infrared imaging in each field of view. (d) Modulation transfer function of the projection optical path. (e) Point diagram of the projection optical path.

**Table 1 Fundus camera design specifications**

Parameter	Value
Overall length/mm	190
Field of view/deg	53
Entrance pupil diameter/mm	2
Wavelength/nm	436 - 656/850
Diopter range/D	- 20 - +20
Modulation transfer function @145 lp/mm	≥0.2

projection spot was sharply formed on the CMOS, yielding a regular spot array on the SHWS (Figure 5a 1) that corresponded to a planar reference wavefront (Figure 5a2) with  $S=0.04$  D (in practice, the measured wavefront is influenced by multiple factors and its defocus value rarely reaches zero). When the system was defocused (Figure 5b), the spot array shifted noticeably (Figure 5b1), and the reconstructed wavefront became distorted with  $S=2.6$  D (Figure 5b2).

By moving the focusing lens continuously, a

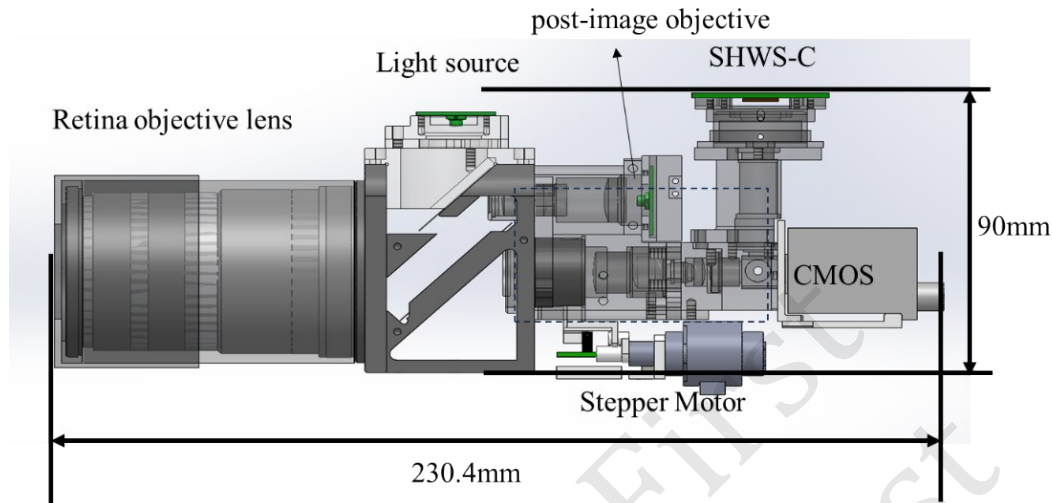


Fig. 4 Fundus camera optical system based on wavefront detection

variation curve of  $S$  versus lens position was obtained, as shown by the red points in Figure 5c. The data exhibit a strong linear correlation, with a coefficient of 0.993 9. This linear and monotonic relationship enables fast, automatic focusing based on the defocus value  $S$ . Given a lens stepping precision of 0.01 mm, the corresponding refractive focusing precision is 0.08D.

For comparison, the conventional method, represented by the black points in Figure 5c, derived from the projection spot size, suffers from a flat zone near the focus, resulting in a positioning precision of only 0.18 mm (refractive precision: 1.44 D). Thus, the proposed wavefront method improves focusing precision by a factor of 18. Additionally, the sign of  $S$  directly indicates the direction of adjustment. The system (with i7-13620H processor) calculates a single-frame image within 10 ms, including centroid detection, Zernike fitting, and focus-step calculation. With a 40 ms image acquisition time per frame, it typically converges within 5 – 9 frames, resulting in a total focusing time under 500 ms, demonstrating high-speed autofocus capability.

To assess the performance across various refractive states, trial lenses ranging from  $-20$  D to  $+20$  D (in 10 D increments) were placed in front of the camera. Figure 5d presents the resulting unfocused fundus images under these refractive conditions. The amplitude contrast (AC)<sup>[24]</sup>, defined as the intensity difference between retinal vessels and the background, remained below 10, rendering fine

structures difficult to discern. Wavefront measurements indicated that positive trial lenses produced convex wavefronts, whereas negative lenses yielded concave wavefronts, with the wavefront distortion increasing with the magnitude of the diopter. Following wavefront-based refocusing (Figure 5e), AC values exceeded 15, indicating a substantial improvement in image sharpness. The reconstructed wavefront became nearly planar, confirming the effectiveness of the correction. Besides, the system demonstrated excellent stability, with a coefficient of variation of only 1.83% in AC over 48 consecutive autofocus tests on a model eye (mean  $AC=8.703$ ,  $SD=0.343$  2), confirming high repeatability and robust long-term performance (as shown in Figure S1).

#### 4.2 Human eye experiments

Human eye experiments were conducted to evaluate the practical performance of the proposed system. A total of 25 volunteers (50 eyes) were enrolled, with the following inclusion criteria: age 18 – 35 years, refractive power between  $+10$  D and  $-15$  D, pupil diameter 3 – 6 mm, and no history of other ocular diseases. The study protocol was approved by the Ethics Committee of Foshan University (approval no. FUME2025022). All imaging was performed under dark conditions.

Among the 50 eyes tested, the projection spot-based method achieved a focusing success rate of only 32 %, with an average 4.25 s. In contrast, the wavefront-sensing method attained a success rate

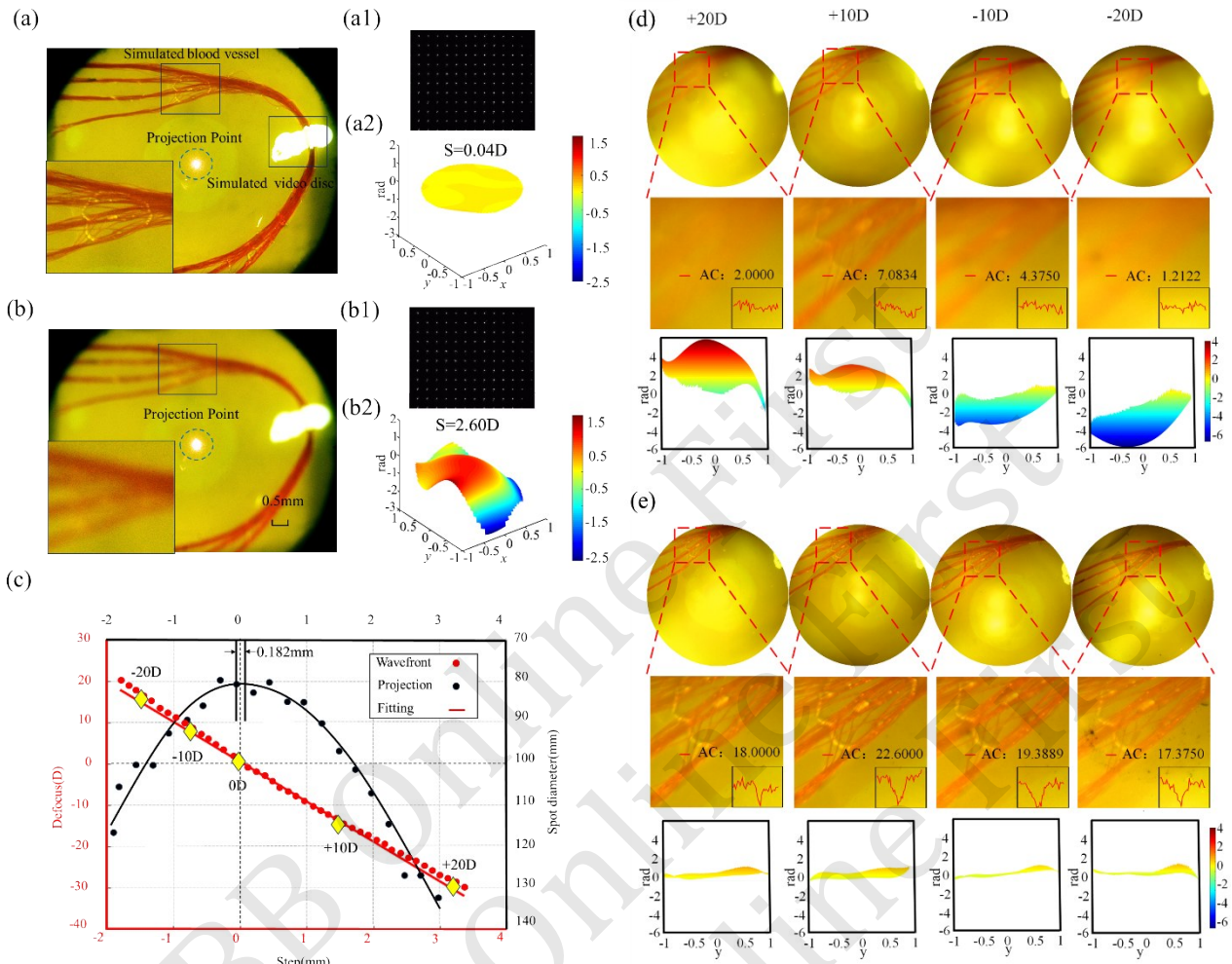


**Fig. 5 Results of model-eye focusing experiments**

(a) Clear model-eye fundus image. a1, corresponding spot pattern; a2, reconstructed wavefront (defocus  $S=0.04$  D). (b) Blurred model-eye fundus image. b1, corresponding spot pattern; b2, reconstructed wavefront (defocus  $S=2.6$  D). (c) Focusing curves obtained by wavefront detection and by the projection spot-size method. (d) Unfocused fundus images under different trial-lens powers (with corresponding amplitude contrast, AC). (e) Refocused fundus images after wavefront-based correction (with corresponding AC values).

exceeding 92 %, with an average of 0.5 s, demonstrating clear advantages in both success rate and operational speed.

Representative cases under stable and unstable imaging conditions were further analyzed. Under stable conditions (Figure 6a), the wavefront method consistently delivered sharp focus, whereas the projection method often yielded slight defocus due to

Our system was compared with two mainstream commercial portable fundus cameras, the Shanghai Yingtong AI-FD16aF and the Shanghai Meowo FC162, both of which adopt projection-based autofocus. The practical imaging speed includes alignment, pupil centering, refractive adjustment, and

its inherent response to the flat zone. During prolonged focusing, which can induce blinking, eye movement, or pupil shift (Figure 6b), the wavefront method completed focusing rapidly, minimizing subject discomfort. By contrast, the projection method was susceptible to eyelid glare and intra-blink light reflections, which degraded image quality.

image acquisition. As summarized in Table 2, our system basically meets the performance standards of commercial devices, has certain advantages in overall imaging speed, demonstrates its potential in practical applications, and provides a new focusing method for portable fundus cameras.

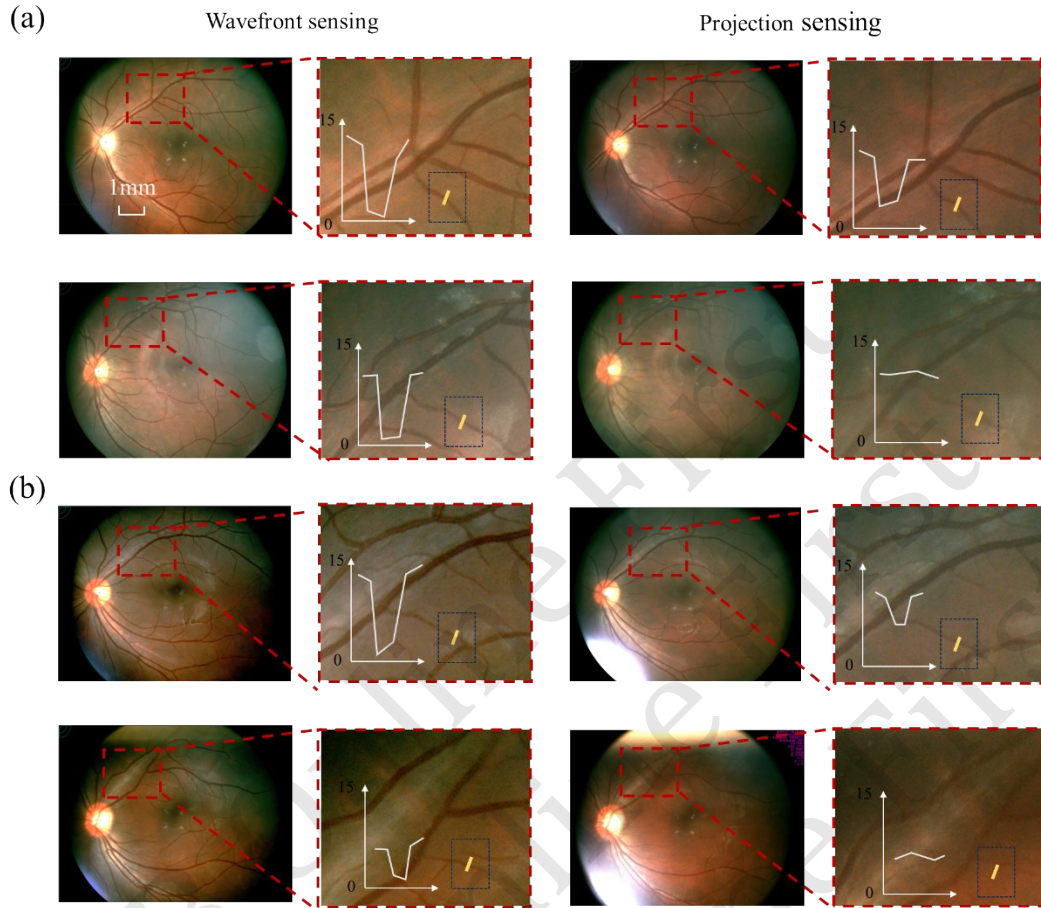


**Fig. 6 Results of automatic focusing of the human eye fundus**

(a) Human eye with steady fixation during imaging. (b) Human eye without steady fixation during imaging. Straight-line interception of secondary blood vessels at the same location to obtain amplitude curves.

**Table 2 Comparison of this system with portable fundus cameras available in the domestic market**

	Our system	AI-FD16aF	FC162
Average focusing time/s	0.5	2.5	2.5
Resolution/ ( $\text{lp}\cdot\text{mm}^{-1}$ )	80	80	80
Field of view/ $^{\circ}$	53	40	50
Range of refractive adjustment/D	-20 - +20	-15 - +15	-20 - +20
Focusing method	Hartmann wavefront sensing	Single-point projection method	Azimuthal projection
Dimensions (L×H) /mm <sup>2</sup>	230×90	280×130	320×125
Pupil diameter/mm	3.2	3.5	3

## 5 Conclusion

In this study, we designed and implemented an autofocus system for portable fundus cameras based on direct wavefront sensing. By integrating a miniaturized SHWS with a collimating lens into the imaging path, the system directly measures the wavefront from a retinal projection spot at the CMOS-

conjugate plane. Wavefront reconstruction via Zernike polynomial yields a quantitative defocus value, which is used to establish a precise defocus to displacement mapping and enables closed-loop autofocus without iterative search. For the first time, SHWS is used as a dedicated defocus sensor to achieve direct focusing in a fully closed-loop manner without iterative searching.

Experimental results show that the system

provides a refractive compensation range of  $\pm 20$  D over a 5 mm focusing travel, with an average total focusing time of 0.5 s and an accuracy of 0.08 D. This approach effectively overcomes key limitations of conventional methods, such as the slow convergence of image-based algorithms and the diffraction sensitivity of projection-based techniques. Evaluations on both model eyes and human eyes confirmed that the system can quickly and stably achieve automatic focusing, obtaining clear fundus images.

In summary, the proposed method achieves a favorable balance of compactness, focusing range, accuracy, and speed, without requiring complex optical components or intensive computation. It thus provides a practical, high-performance focusing solution for portable fundus cameras. It should be noted, however, that to advance this method toward practical application and commercialization, further efforts will be needed to optimize system cost, power consumption, and adaptability to challenging ocular condition, such as dense cataracts or small pupils. These aspects represent important directions for future research.

**Supplementary** Available online (<http://www.pibb.ac.cn>, <http://www.cnki.net>):

PIBB\_20250491\_Figure S1.pdf

PIBB\_20250491\_Table S1.pfd

### References

- [1] Poplin R, Varadarajan A V, Blumer K, *et al.* Prediction of cardiovascular risk factors from retinal fundus photographs via deep learning. *Nat Biomed Eng*, 2018, **2**(3): 158-164
- [2] Das S, Kuht H J, de Silva I, *et al.* Correction: Feasibility and clinical utility of handheld fundus cameras for retinal imaging. *Eye (Lond)*, 2023, **37**(2): 380-381
- [3] Wang S, Jin K, Lu H, *et al.* Human visual system-based fundus image quality assessment of portable fundus camera photographs. *IEEE Trans Med Imaging*, 2016, **35**(4): 1046-1055
- [4] Jin K, Lu H, Su Z, *et al.* Telemedicine screening of retinal diseases with a handheld portable non-mydratric fundus camera. *BMC Ophthalmol*, 2017, **17**(1): 89
- [5] Panwar N, Huang P, Lee J, *et al.* Fundus photography in the 21st century—a review of recent technological advances and their implications for worldwide healthcare. *Telem J E Health*, 2016, **22**(3): 198-208
- [6] Chen J, Zheng S, Pan L, *et al.* Fine and rough combined auto-focusing method for non-mydratric fundus camera. *Acta Opt Sin*, 2014, **34**(11): 1110003
- [7] 赵玉玲. 一种手持式眼底相机的自动对焦方法及系统: 中国, 202310807254.3. 2023-09-26
- [8] Liu Z, Qiu S, Cai H, *et al.* Enhancing autofocus in non-mydratric fundus photography: a fast and robust approach with adaptive window and path-optimized search. *Appl Sci*, 2023, **14**(1): 286
- [9] 陈志, 陈大伟, 龚明利, 等. 自动对焦的眼底相机: 中国, 201911397588.8. 2021-08-17
- [10] Chen Z, Chen D W, Gong M L, *et al.* Fundus camera with automatic focusing: China, 201911397588.8. 2021-08-17
- [11] 尉佩, 陈嘉轩, 袁夏冰, 等. 一种眼底快速定焦系统: 中国, 202410321918.X. 2024-05-17
- [12] Wei P, Chen J X, Yuan X B, *et al.* Rapid focusing system for fundus imaging: China, 202410321918.X. 2024-05-17
- [13] 牟国强, 陈荡荡, 杨皓聿. 一种用于眼底相机调焦的光学系统及眼底相机: 中国, 202410579696.1. 2024-07-02
- [14] Mou G Q, Chen D D, Yang H Y. Optical focusing system for fundus camera and fundus camera using the same: China, 202410579696.1. 2024-07-02
- [15] Rao D P, Negiloni K, Gurunathan S, *et al.* Validation of a simple-to-use, affordable, portable, wavefront aberrometry-based auto refractometer in the adult population: a prospective study. *BMC Ophthalmol*, 2022, **22**(1): 498
- [16] 舒衍, 柯程虎, 柯熙政. Zernike多项式拟合人眼波前像差研究进展. *激光技术*, 2025, **49**(5): 769-776
- [17] Shu Y, Ke C H, Ke X Z. *Laser Technol*, 2025, **49**(5): 769-776
- [18] Balas M, Ramalingam V, Pandya B, *et al.* Adaptive optics imaging in ophthalmology: redefining vision research and clinical practice. *JFO Open Ophthalmol*, 2024, **7**: 100116
- [19] Deng Y, Zhao J, Dai Y, *et al.* Simultaneous quantification of longitudinal and transverse ocular chromatic aberrations with Hartmann-Shack wavefront sensor. *J Innov Opt Health Sci*, 2018, **11**(4): 1850021-1-1850021-11
- [20] Ren J, Yin Q, Fu P, *et al.* A compact fundus image guided adaptive optics scanning laser ophthalmoscope (AOSLO) imaging system with active eye tracking designed for clinical use. *Invest Ophthalmol Vis Sci*, 2024, **65**(7): 4
- [21] Kong W, Chen Y, Shi G, *et al.* Imaging of human parafoveal area with large field of view in adaptive optics line scanning ophthalmoscope. *J Innov Opt Health Sci*, 2024, **17**(6): 2450008
- [22] Jiang H, Li C, Liao N, *et al.* Optical design of adaptive optics scanning laser ophthalmoscope with adjustable focus. *Laser Optoelectron Prog*, 2019, **56**(2): 022202
- [23] Li C C, Gong Y, Li J, *et al.* Optical system design of a fundus camera capable of inducing automatic focusing of the human eye. *Acta Optica Sinica*, 2014, **34**(4): 7
- [24] Bao M D, Shi G H, Xing L N, *et al.* High-precision spherical wavefront calibration method for shack-hartmann wavefront sensor. *Chin Optics*, 2024, **17**(3): 521-527
- [25] Wyant J C, Creath K. Basic wavefront aberration theory for optical metrology. *Appl Optics Opt Engineer*, 1992, **11**(2): 28-39
- [26] Liang J, Grimm B, Goelz S, *et al.* Objective measurement of wave aberrations of the human eye with the use of a Hartmann-Shack wave-front sensor. *J Opt Soc Am A Opt Image Sci Vis*, 1994, **11**(7): 1949-1957
- [27] Lapointe N, Akitegetse C, Poirier J, *et al.* Targeted spectroscopy in the eye fundus. *J Biomed Opt*, 2023, **28**(12): 126004
- [28] Wang Y, Wang R K. High-resolution computed tomography of refractive index distribution by transillumination low-coherence interferometry. *Opt Lett*, 2010, **35**(1): 91-93

# 基于夏克-哈特曼波前传感的紧凑型快速自动对焦眼底成像系统\*

陈隆\*\* 林哲凯\*\* 郑庚泳 黄金天 董佳鑫 杨尚潘 丁文正  
曾亚光 王雪花\*\*\* 韩定安\*\*\*

(佛山大学物理与光电工程学院粤港澳智能微纳光电技术联合实验室, 佛山 528225)

**摘要** **目的** 为解决便携式眼底相机自动调焦技术存在的精度低、速度慢及系统复杂等问题, 本文提出了一种基于波前探测的自动调焦方法。**方法** 该自动调焦方法向眼底投射光点, 并利用微型夏克-哈特曼波前传感器采集像面聚焦点的波前信息; 通过Zernike多项式对波前相对于参考面的离焦量进行量化, 进而驱动调焦镜完成闭环对焦。**结果** 基于此方法, 设计并搭建了一套紧凑型眼底成像系统。测试结果表明, 该系统在5 mm的调焦行程内, 可实现 $\pm 20$  D的屈光补偿范围, 调焦精度优于0.08 D, 单次调焦时间小于0.5 s。**结论** 在模拟眼与真人眼实验中, 该系统均表现出快速、高精度的自动调焦性能, 验证了其作为便携式眼底相机自动调焦解决方案的有效性。

**关键词** 便携式眼底相机, 自动调焦, 波前探测, 夏克-哈特曼波前传感器

中图分类号 TP272, R774

DOI: 10.3724/j.pibb.2025.0491

CSTR: 32369.14.pibb.20250491

\* 国家自然科学基金(62205060, 62075042)和粤港澳智能微纳光电技术联合实验室研究基金(2020B1212030010)资助项目。

\*\* 并列第一作者。

\*\*\* 通讯联系人。

王雪花 Tel: 18718560259, E-mail: xhwang10000@163.com

韩定安 Tel: 15118799767, E-mail: handingan@163.com

收稿日期: 2025-11-05, 接受日期: 2026-02-11